LHC-B/97-018
RICH
05/11/97

Particle Identification in the RICH Detectors and Study of Impact Parameters

André Schöning
CERN, Geneva

Abstract

The particle identification in the RICH detectors using the so called "local approach" pattern recognition is described. Results of the RICH simulation and the reconstruction of Cherenkov angles are shown. The pattern recognition efficiency is presented and requirements on impact parameters from the tracking system are quoted.

Introduction

The experiment LHC-B has been proposed [1] to measure CP violation and $b\bar{b}$–mixing at the Large Hadron Collider (LHC). The installation of two RICH detectors is planned to provide a highly efficient particle identification. In this note the strategy for particle identification and the pattern recognition of Cherenkov ring images is described. This analysis is based on the full simulation of Cherenkov photons and their tracking through the detector, taking in account the proposed detector layout in [1] and all detection efficiencies.

The pattern recognition method proposed in this note makes use of the so called "local approach", in which the pattern recognition of individual ring images are treated independently. A local log–likelihood function is used to distinguish between different particle hypothesis. Another, so called "global fit" method, has been proposed [2], in which hit–track assignments are performed by using a global fit. In this approach each photon is explicitly assigned to a reconstructed ring image using a global log–likelihood function. For both methods the performance of the pattern recognition relies on the knowledge of the track parameters measured in the tracking system. The dependence of the particle identification performance on the track resolution is studied here and limits on the required track resolution for the RICH pattern recognition are given.

At the LHC-B experiment additional information on particle identification is supported by the calorimetric system (e/h separation) and by the muon system (μ identification). In the present note only particle identification in the the RICH detectors is considered and information from other detectors other than the tracking system is not taken into account.

RICH System

The LHC-B RICH system consists of two stations of RICH detectors. The first station (RICH1) is located $1 - 1.95\ m$ downstream of the nominal pp interaction point. It is placed directly behind the position of the silicon vertex detector. The second RICH station (RICH2) is located about $9.6 - 11.2\ m$ downstream of the the pp interaction point. In between, a system of tracking detectors and a dipole magnet serve as a spectrometer to provide track position and track momentum information.

In the RICH system different radiator materials are used for the production of Cherenkov rings to provide particle information in a large momentum range of about $1 - 150\ GeV$. For the RICH1 detector both aerogel ($\gamma_{threshold} = 3 - 4$) and C_4F_{10} gas ($\gamma_{threshold} = 19$) are foreseen to detect ring images from both low and high momentum particles. The angular acceptance of the first station is $\vartheta < 330\ mrad$. For the second RICH2 station, which covers $\vartheta < 120\ mrad$, CF_4 gas ($\gamma_{threshold} = 33$) is planned to be used.

A system of focussing mirrors (oriented symmetrically with respect to the horizontal axis) reflects the Cherenkov light onto two systems (left/right from the detector) of Pixel/Pad–HPDs (Hybrid Photon Detector) [3] at both stations. The HPDs are designed for the detection of single photons in the energy range of $2 - 5\ eV$. The pixel size of $2\ mm \times 2\ mm$ is a compromise between the required resolution and the number of readout channels. Each HPD system consists of about 30-40 HPDs and the total size is ($720\ mm \times 600\ mm$). The coverage of the HPD system by active photon detectors is about 70% and is determined by the size of the uninstrumented region between the circular photocathodes, which are arranged in a hexagonal matrix.

Simulation

Results presented in this note take into account a full simulation [4] of detector acceptances, smearing effects and photon detection efficiencies. The inefficiency due to the uninstrumented regions is currently taken into account by a global correction. The main smearing effects, which contribute to the resolution of the reconstructed mass, are the unknown emission point of the photon, the chromatic aberration in

Detector	RICH1		RICH2
Radiator	aerogel	C_4F_{10}	CF_4
$\gamma_{threshold}$	$3-4$	19	33
r_n refraction index	1.03	1.0014	1.0005
ϑ_{max} $/rad$	0.2427	0.0526	0.0314
$length_{radiator}$ $/cm$	5.0	≈ 88.0	≈ 160.0
tracks / event	36		46
ring images / event	31.2	19.5	39.7
HPD hits / event	420	770	950
HPD hits /ring image	13.5	39.4	24.0
σ_ϑ $/mrad$	1.3(*114)	1.1	0.33

Table 1: *Summary of the design parameters and characteristics of the RICH detectors and radiator materials. In addition, RICH simulation results and the expected resolution of the Cherenkov angle measurement are given. For simulation a MC sample including $B \to \pi\pi$ decays has been taken. (*) The value in brackets is the RMS of the distribution, which is much larger than the fitted peak resolution due to Rayleigh scattering of about one third of all photons.*

the radiator material, the granularity of the pixel HPD and the Rayleigh scattering in aerogel. The position and momentum of the charged tracks producing Cherenkov light are assumed to be perfectly determined by the tracking system. The influence of the experimental resolution on this is studied in the last section of this paper.

For illustration, a typical simulated hit distribution registered by the HPD–system in RICH1 and RICH2 is shown in Fig. 1 a) and b) for a simulated event, which contains a $B \to \pi\pi$ decay. Some of the Cherenkov ring images can be clearly identified by eye. In the RICH1 detector concentric ring images with very different radii are registered. The smaller ones are produced in the gas radiator and the larger ones are produced in aerogel.

The distributions of the number of hits per ring and of the Cherenkov angles are shown in Fig. 2 for simulated electrons and pions passing the RICH1 aerogel, RICH1 gas and the RICH2 gas radiator. The mean hit number per track measured in the RICH detectors for a simulated $B \to \pi\pi$ sample are $\bar{n}_{hit} = 13.5$ for aerogel, $\bar{n}_{hit} = 37$ for C_4F_{10} and $\bar{n}_{hit} = 24$ for CF_4. The maximum Cherenkov angle θ_{max} is given by the refraction index and varies for the different radiator materials. The maximum Cherenkov angle and some additional simulation results are given in Table 1 for the three radiator materials.

Reconstruction of Cherenkov angles

The Cherenkov angles of photons registered in the HPD are calculated in two steps. In the first step, hits of both HPD systems are checked if they can be traced back to the considered track within the active radiator volume. In the second step, the emission angle of the photon is calculated with respect to the expected mean emission point. For some tracks, hits in both HPD systems are be found. Even photons originating from the same track and all emitted into the same direction are expected in different HPD systems, depending on the point of photon emission.

The resolution of the photon angle reconstruction depends on several smearing effects. Fig. 3 a) shows the reconstructed photon angle taking into account only the smearing due to the granularity of the pixel HPD. Fig. 3b) shows the smearing of the reconstructed photon angle due to the uncertainty of the position of the true photon emission point. Fig. 3c) shows the corresponding smearing of the Cherenkov angle due to the chromatic aberration in the radiator. In Fig. d) the sum of all these smearing effects is shown. The additional broadening of the photon angle resolution in aerogel due to Rayleigh scattering is shown in Fig. e). The angular resolution for reconstruction of the Cherenkov angle for the three different radiators is also listed in Table 1.

The photon angle resolution can be transformed into an equivalent mass resolution as function of γ of the particle by using the equation:

$$\frac{\delta m}{m} = \gamma^2 \; \beta \; r_n \, \delta\vartheta_{Cherenkov}/\sqrt{C} \; , \tag{1}$$

with r_n the refraction index of the radiator material and C a constant parameter. The mass resolution as expected from the precision of the $\vartheta_{Cherenkov}$ measurement is shown in Fig. 4 as a function of γ for all three radiators. The thresholds γ_{thresh}, at which Cherenkov rings start to be produced, are given by the left edges of the distribution. The relative mass error takes into account the $\vartheta_{Cherenkov}$ measurement as well as the number of measured hits per ring image, which enter into the constant C.

Pattern Recognition

Two different strategies for pattern recognition have been developed. In the "local approach" method the Cherenkov rings produced by charged tracks are found independently. Hits produced by other tracks not belonging to the considered track are an "intrinsic" background source. In the "global fit" method [2] all hits are assigned to charged particles at the same time by taking into account all particle hypotheses. Particles are identified by the hypothesis with the best global fit. In the following section the local approach method is described in more detail.

The "local approach" method

For all measured tracks in the tracking system, different particle hypotheses (e, μ, π, K and p) are made. A ring image with the expected Cherenkov angle $\vartheta_{hypo} = \vartheta(m_{hypo})$ for a given particle hypothesis is searched in the registered HPD hit pattern. For each considered track, which has been measured in one of the tracking detectors, a log–likelihood function $\mathcal{L}$ can be defined as function of the Cherenkov angle:

$$\mathcal{L} = \frac{1}{N} \sum_{hits\ i} \log \left(1 + \frac{1}{\sqrt{2\pi}\sigma_\vartheta \varepsilon} e^{-\frac{(\vartheta_i - \vartheta_{hypo})^2}{2\sigma_\vartheta^2}} \right) \tag{2}$$

$$N = \log \left(1 + \frac{1}{2\sqrt{\pi}\sigma_\vartheta \varepsilon} \right) , \tag{3}$$

where ϑ_i is the reconstructed emission angle of the photon, calculated with respect to the direction of the considered track. σ_ϑ is a parameter describing the angular resolution and ε is a hit selection parameter, which defines an effective bandwidth around the considered Cherenkov angle ϑ_i. N is a normalisation parameter, which ensures that the value of the log–likelihood function corresponds to the number of hits contributing to a certain ϑ_i, according to the angular resolution σ_ϑ. The sum is performed over all hits but is restricted for practical reasons (after a preselection of hits to save CPU time) to hits with $\vartheta_i \lesssim \vartheta_{max}$, where ϑ_{max} is the limit for infinitely high momentum particles.

The log–likelihood function is now used to calculate the number of hits n, which can be attributed to a given mass hypothesis m_{hypo}. The log–likelihood is evaluated at the mean photon emission angle, taking into account the achromatic aberration in the radiators. It is calculated by integrating over the energy window, in which the HPD are sensitive to photons:

$$\vartheta_{hypo} = \frac{\int dE_\gamma \, \frac{dn_\gamma}{dE_\gamma} \, \vartheta(m, E_\gamma)}{\int dE_\gamma \, \frac{dn_\gamma}{dE_\gamma}} \, . \tag{4}$$

The reconstructed number of hits $n = \mathcal{L}(\vartheta_{hypo})$ is compared to the number of expected hits n_{hypo}, which is given by:

$$n_{hypo} = \int dE_\gamma \frac{dn_\gamma}{dE_\gamma} A \cdot D \, , \tag{5}$$

where A is the geometrical acceptance and D the total detection efficiency. Finally, a probability $prob_{hypo} = Poisson(n, n_{hypo})$ for this interpretation is calculated, which will be used in the following to discriminate between different particle hypothesis.

For illustration, Fig. 5 a) shows the log–likelihood function as function of ϑ for track 1 in Fig. 1b). The ϑ_{hypo} values for the different particle hypothesis are indicated by lines. The points show the expected number of hits for each particle hypothesis.

The influence of the parameter ε and σ_ϑ on the log–likelihood function is demonstrated in Figs. 5 b-e), in which the function $\mathcal{L}(\vartheta)$ is shown for the same track as in Fig. 5 a) but for different parameter sets of ε and σ_ϑ. For small values of σ_ϑ, which corresponds to a underestimation of the Cherenkov angle resolution, the distribution shows a discrete spectrum of individual hits. For large values of σ_ϑ, which corresponds to a overestimation of the Cherenkov angle resolution, the peak is broadened and smeared out.

As described above, ε is essentially an effective cut parameter. It determines for each hit a weighting factor of its contribution to the log–likelihood as function of its deviation from the considered angle ϑ_{hit}. In the limit $\varepsilon \to \infty$ (Fig. 5 d) the log–likelihood is proportional to $\sum_{hits} e^{-\frac{(\vartheta_{hit}-\vartheta_{hypo})^2}{2\sigma_\vartheta^2}}$. Essentially, only hits with $|\vartheta_{hit} - \vartheta_{hypo}| \lesssim \sigma_\vartheta$ contribute. In the limit $\varepsilon \to 0$ (Fig. 5 e) all measured hits contribute with equal weights, resulting in a parabolic log–likelihood : $\mathcal{L} \propto -\sum_{hits} \frac{(\vartheta_{hit}-\vartheta_{hypo})^2}{\sigma_\theta^2}$, with one peak located in the mean position of all hits. In this note $\varepsilon = 1$ is chosen, which gives reasonable results as will be shown in the following section.

Ideal case

The resulting probabilities for generated e, μ, π, K and p particles are shown in Fig 6. To demonstrate the method, the probabilities are given for the ideal case of having only a single ring image per event. The probabilities are calculated for both the e and π interpretation. The shaded histogram shows the distribution if the e and π interpretation is correct, the solid line shows the distribution if the e and π interpretation is wrong. For the correct interpretation the distribution is flat, as expected, while the wrong interpretation has a peak at zero.

The figures show that just by cutting on the probability the particles cannot be separated completely. This is the case especially for high momentum particles, because for these particles similar Cherenkov angles are expected. Discrimination between the different particle hypotheses is achieved by choosing the interpretation, which gives the highest probability. In addition, the log–likelihood function of the hypothesis has to satisfy a peak finder at ϑ_{hypo}.

The resulting particle identification efficiencies are given in Tables 5 a,b) for the RICH1 and RICH2 detectors. The table shows the number of identified and misidentified e, μ, π, K and p particles. Because a minimum probability of $prob > 0.001$ is required, a small fraction of particles is not identified. Not identified particles are given in the last line labelled with "X". The efficiencies are defined as the ratio of correctly identified particles to the number of generated particles. The tables give also the purity, which is defined as the ratio of correctly identified particles to the

radiator:	aerogel	C_4F_{10}	CF_4
ε	1.0	1.0	1.0
σ_ϑ /$mrad$	0.76	0.54	0.13

Table 2: *Final parameters used for the pattern recognition in the RICH detectors.*

total number of identified particles for each interpretation.

The resulting efficiencies for the correct particle identification are well above 90% apart for muons, which are often identified as pions due to their similar mass. The inefficiencies come mainly from imperfections of the experimental setup and from the detector resolution. Because the ideal case of having only one ring image has been investigated here, no wrong hit–track assignments are made. Therefore these efficiencies represent an upper limit for a perfect pattern recognition in a real environment. In a real environment, apart from the intrinsic background, additional hits from other sources like noise and backscattered particles make the pattern recognition more difficult, which is not considered here.

Realistic case

The pattern recognition is now repeated by considering all tracks of simulated $B \to \pi\pi$ events simultaneously. The pattern recognition has now to deal with additional hits from neighbouring ring images (intrinsic background). Figs. 6 c,d) show the probability distribution for the e, π interpretation of e, μ, π, K, p particles. Due to additional hits from the intrinsic background the probabilities are now overestimated. The signal distribution (correct interpretation) as well as the background distribution (wrong interpretation) show a peak at $prob \sim 1$.

This effect can be compensated by tuning the parameter σ_ϑ. By choosing a smaller value the angular resolution is artificially overestimated and the signal–to–background ratio is improved. The compensation is illustrated in Figs. 6 e,f). In the following, the parameter σ_ϑ "tuned" to a more realistic case is used. The final parameters used for the pattern recognition in the detectors are given in Table 2. Quantitative results on the pattern recognition efficiencies are discussed in the next section.

Results for $B \to \pi\pi$ decays

In this section results on the pattern recognition efficiency are presented for simulated events, which contain $B \to \pi\pi$ decays. The $B \to \pi\pi$ decay sample has been chosen for physics motivation. Furthermore, it is expected that all results presented in this note hold also for other B decays as well as for common pp processes, because most particles detected in the RICH detectors are produced by light quarks.

Table 5 c–f) show the efficiencies for the correct particle identification using the "local approach" pattern recognition described in the last section. The last column shows the number of charged particles, which do not produce any Cherenkov rings (defined as $N_{hit} < 3$), in addition to Tables 5 a,b). By chance these tracks can be attributed to hits belonging to ring images of other tracks and thus lead to an accidental particle identification. These tracks are treated separately in the table and labelled with "X".

The results are given for all three radiators: Table 5 c) RICH1 gas, d) RICH2 gas and e) RICH1 aerogel. The pattern recognition efficiencies for the gas radiators are $70 - 100\%$ and are very close to the ideal case of a perfect pattern recognition (Tables 5 a,b). Despite the overlays of gas and aerogel ring images the pattern recognition efficiency of gas ring images is not very much affected by the additional aerogel rings. In contrast, the pattern recognition efficiency of aerogel ring images is affected by the additional gas rings, which have a high photon multiplicity compared to the low photon multiplicity from aerogel. The pattern recognition efficiency of aerogel ring images is about $45 - 85\%$. An additional reason for the moderate efficiency is the bad angular resolution due to multiple scattering in aerogel that reduces the effective number of hits, which enter into the log–likelihood .

Therefore, the pattern recognition can be improved by removing hits, which have already been identified as gas images. In a second step, the pattern recognition is performed on the remaining hits, which should be originated from the aerogel radiator. The resulting pattern recognition efficiency, given in Table 5 f), is typically $55 - 95\%$.

Finally, all results of the individual measurements are combined by calculating an average probability for all particle hypothesis and by choosing the interpretation with the highest probability. The combined pattern recognition efficiency of the RICH1 and RICH2 gas radiators is given in Table 6 a). The combined result including the aerogel information is given in Table 6 b). The final efficiencies are between $80 - 100\%$, depending on the particle type, and the purities are between $70 - 100\%$, apart for muons due the the large background from misidentified pions. The tables show that by including the aerogel information the particle identification efficiency and the purity is improved. Also the number of tracks with no ring images is significantly reduced.

The momentum dependence of the pattern recognition efficiency is shown in Fig. 7 a) for all particle interpretations. The pattern recognition efficiency decreases at high momenta for low mass particles (e,μ,π) whereas the efficiency for heavy particles (K,p) is small at small momenta, due to the higher threshold, and increases with high momenta.

radiator:	aerogel	aerogel w/o C_4F_{10}	C_4F_{10}	CF_4	total
time $/sec$	2.3	0.9	0.7	0.8	2.4

Table 3: *Processing time of the angle reconstruction and pattern recognition for ring images from the different radiator materials.*

Noise

The effect of random noise can be seen in Fig. 7 b). The particle identification efficiency is plotted against the noise rate of the pixels, which fire randomly. Small effects can be seen for a noise rate larger than 0.01. Below this rate noise has no significant effect on the pattern recognition.

Performance

All studies have been made on a HP9000/B132 workstation. The average time used for the reconstruction and pattern recognition of the total event is 2.4 sec without optimising the code for a fast reconstruction. Most time is used for the reconstruction of the Cherenkov angle, for which the HPD hits of a ring image have to be extrapolated back to the candidate track. Table 3 shows the processing time for the aerogel, C_4F_{10} and CF_4 hits. The processing of the aerogel hits is much faster (and more efficient), if the identified C_4F_{10} are removed before pattern recognition. This time enters into the total time, which is given in the last column.

Requirements on Impact Parameters

The particle identification with the RICH system relies on track parameters measured in the LHC-B tracking system. The resulting requirements for the design of the LHC-B experiment and in particular of the tracking system are discussed in this section.

Information on the particle direction is required to provide an assignment of particles and ring images. The requirements on the knowledge of the impact point (x_0, y_0) on the RICH detectors and the the particle direction (φ, ϑ) are low because these parameters do not enter directly into the calculation of the Cherenkov angle. On the other hand these parameters have to be measured with sufficient precision to enable an assignment of tracks and ring images.

The opening angle of the ring image has to be converted into a particle mass by making use of the measured momentum of the particle. Therefore, a precise knowledge of the track momentum is required. The particle momenta are determined

κ	$\lesssim 3 \cdot 10^{-4}\ GeV^{-1}$
Δx_0	$\lesssim 0.3\ cm$
Δy_0	$\lesssim 1.0\ cm$
$\Delta \vartheta$	$\lesssim 0.3\ mrad$
$\Delta \varphi$	$\lesssim 3.0\ mrad$

Table 4: *Requirements on track impact parameters. The track momentum error is parameterised as:* $\Delta p/p = \kappa\ p$.

by their bending radii in a magnetic field of 1.2 T and the momentum resolution is parametrised as $\Delta p/p = \kappa\ p$.

The pattern recognition efficiency as function of the track parameter resolution $\Delta x_0, \Delta y_0, \Delta\vartheta, \Delta\varphi$ and κ is shown in Fig. 8 for the combined measurement. From these plots, limits on the acceptable resolution on track parameters can be derived, such that the pattern recognition efficiency in the RICH detectors is not significantly affected. The requirements are summarised in Table 4. The tightest requirement is set on the track momentum resolution of $\Delta\kappa \lesssim 3 \cdot 10^{-4} GeV^{-1}$.

Conclusions and Outlook

The pattern recognition program described in this note using the "local approach" method provides a highly efficient e/π separation as well as a highly efficient K, p identification with purities of about 70%. The program is relatively fast and not very sensitive to noise. The "local approach" method allows a particle identification on a single track basis that makes this method attractive for trigger applications.

For the future the following items are planned to be investigated:

- reduction intrinsic background by using the "local approach method" in an iterative procedure.
- determination the pattern recognition efficiency for the real hexagonal HPD pattern and design.
- speed up the algorithm.
- trigger feasibility studies.

References

[1] LHC-B Letter of Intent, "A dedicated LHC collider beauty experiment for precision measurements of CP violation", CERN–LHCC/95-5, (Aug. 1995).

[2] *R.Forty,* "Status and plan of R&D for the RICH detectors of LHC-B", CERN/LHCC 96–38, (Oct. 1996).

[3] *E.Chesi et al.,* "Performance of a 256 Pad Hybrid Photon Detector for Ring Imaging", LHCB 96–06, (Oct. 1996).
E.Chesi et al., "Performance of Si Pad Sensors for a RICH Detector", LHCB 96–07, (Oct. 1996).

[4] *Roger Forty,* "RICH Simulation", talk given in the RICH meeting, (Jan. 1997).
Roger Forty, fortran routine PATTERN, private communication, (Feb. 1997).

a) RICH1 C_4F_{10}

	generated					
rec.	e	μ	π	K	p	pur.
e	1733		5			100%
μ	24	36	16			47%
π	16	30	5167			99%
K	6	2	198	259		56%
p			71	6	69	47%
X	35	2	46	2	1	99%
eff.	96%	51%	94%	97%	99%	

b) RICH2 CF_4

	generated					
rec.	e	μ	π	K	p	pur.
e	7233	5	198			97%
μ	33	144	299			30%
π	17	13	7344	4		100%
K	3	1	105	617		85%
p		1	7	1	242	95%
X	52	2	58	13	8	95%
eff.	99%	87%	92%	97%	97%	

c) RICH1 C_4F_{10}

	generated						
rec.	e	μ	π	K	p	X	pur.
e	477	1	29			7	93%
μ	4	17	40			59	14%
π	2	3	1214	1		13	98%
K		1	32	51		6	57%
p			15	1			53%
X	13		25	1	18	1577	98%
eff.	96%	77%	90%	94%	100%	95%	

d) RICH2 CF_4

	generated						
rec.	e	μ	π	K	p	X	pur.
e	1659	3	143			19	91%
μ	13	36	115			19	20%
π	8	9	1666	2		5	99%
K	3	1	44	139		8	71%
p			21	6	63	1	69%
X	18	2	16	1	3	571	93%
eff.	98%	71%	83%	94%	95%	92%	

e) RICH1 aerogel

	generated						
rec.	e	μ	π	K	p	X	pur.
e	434	10	274	12	4	102	52%
μ	26	19	193	9	1	54	6%
π	17	9	1367	8	2	43	95%
K	9	2	238	120	12	12	31%
p	9	1	201	17	62		21%
X	16		41	5	1	260	80%
eff.	85%	46%	59%	70%	76%	55%	

f) RICH1 aerogel without C_4F_{10} hits

	generated						
rec.	e	μ	π	K	p	X	pur.
e	463	7	248	9	9	43	60%
μ	19	23	163	4		45	9%
π	8	9	1618	7	1	26	97%
K	2		157	137	7	8	44%
p	4		87	10	70		41%
X	15	9	41	4	1	349	85%
eff.	91%	56%	7%0	80%	85%	74%	

Table 5: *Pattern recognition efficiency of e, μ, π, K and p particles. The columns correspond to the number of generated particles, the lines to the number of identified particles. The efficiencies of identifying the correct interpretation are given in the bottom line, the purities are given in the last column. a,b) show the result of the ideal case of having only one track for C_4F_{10} and CF_4. c,d,e,f) refer to C_4F_{10}, CF_4, aerogel and aerogel after removing identified C_4F_{10} hits.*

a) C_4F_{10} and CF_4 combined

	generated						
rec.	e	μ	π	K	p	X	pur.
e	2129	3	147			26	92%
μ	13	49	121			77	19%
π	9	9	2441	3		18	98%
K	3	2	60	165		13	68%
p			35	9	75	1	63%
X	31	2	35	1	2	2089	97%
eff.	97%	75%	86%	93%	97%	94%	

b) C_4F_{10}, CF_4 and aerogel combined

	generated						
rec.	e	μ	π	K	p	X	pur.
e	2145	3	149			55	91%
μ	17	68	162			52	23%
π	13	9	3301	4		34	98%
K	3	1	95	275	10	16	69%
p	1		39	10	128	1	72%
X	21	3	52	6	3	875	91%
eff.	98%	81%	87%	93%	91%	85%	

Table 6: *Final pattern recognition efficiency of e, μ, π, K and p particles. The columns correspond to the number of generated particles, the lines to the number of identified particles. The efficiencies of identifying the correct interpretation are given in the bottom line, the purities are given in the last column. a) shows the combined result of taking C_4F_{10} and CF_4 hits. b) shows the final result after combining C_4F_{10}, CF_4 and aerogel hits.*

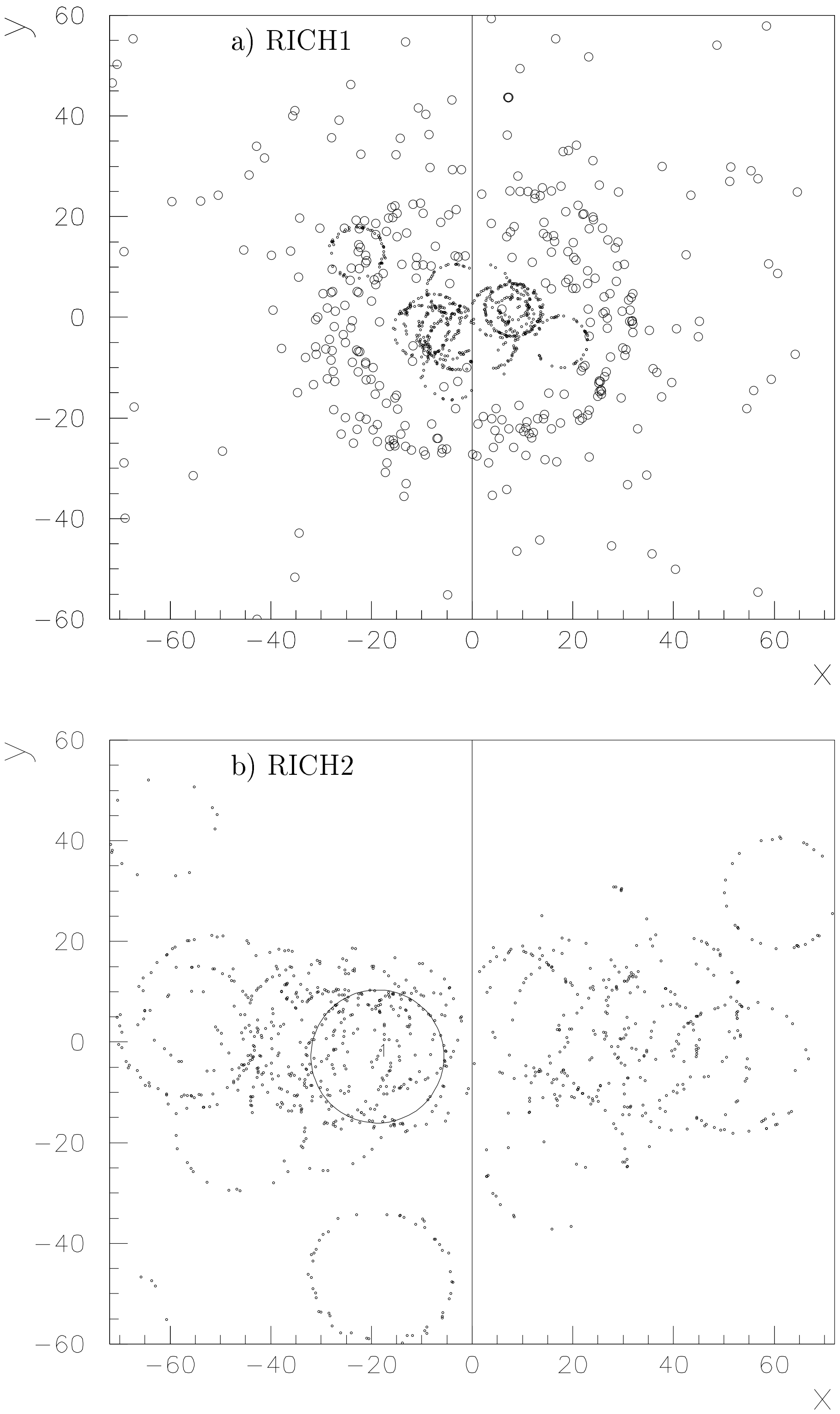

Figure 1: *Simulated hit pattern in the a) RICH1 and b) RICH2 detectors. Photon hits coming from aerogel are plotted as open circles (RICH1). Hits coming from gas radiators are plotted as points.*

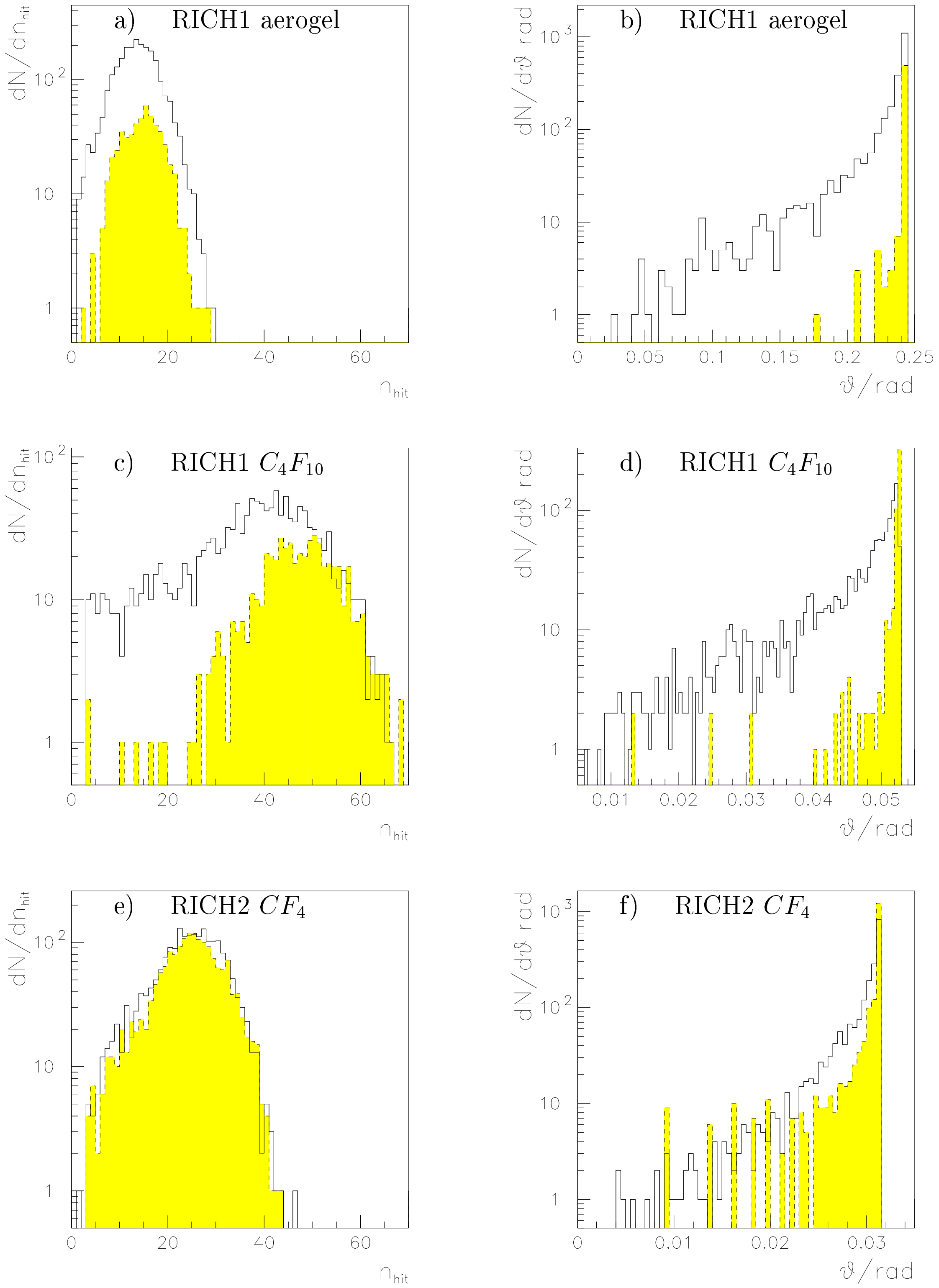

Figure 2: *a,c,e) distribution of number of hits per e (shaded) and π (solid line) particles. b,d,f) distribution of the Cherenkov angle for e (shaded) and π (solid line) particles. Figures a,b) refer to the RICH1 aerogel radiator, c,d) to the RICH1 gas radiator and e,f) to the RICH2 gas radiator.*

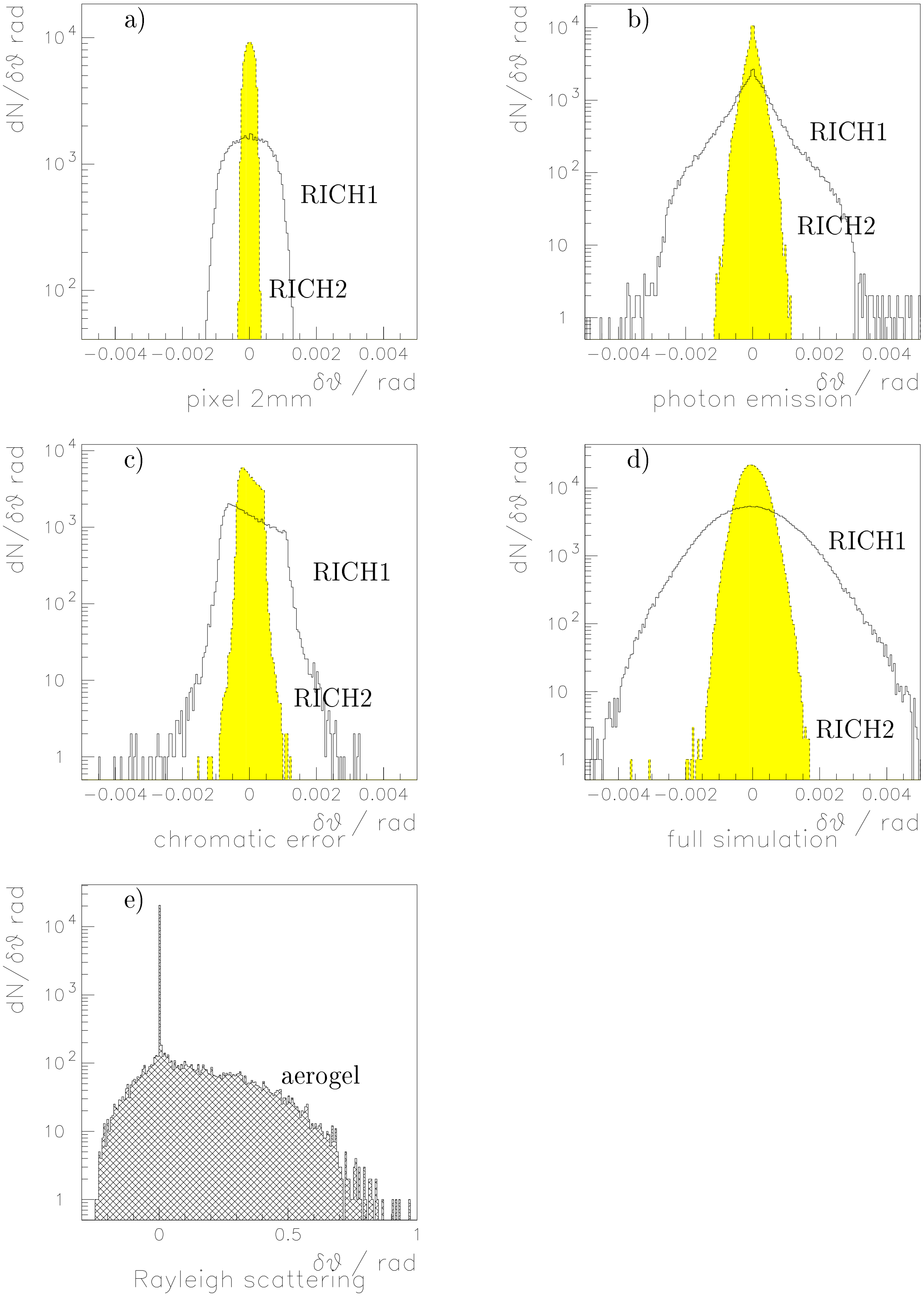

Figure 3: *Different smearing effects for the measured Cherenkov angle in the RICH1 (full line) and RICH2 (shaded) gas radiator. Only one effect is shown at each time in figures a,b,c). Figure d) shows the sum of all effects. Figure e) shows the additional* ϑ *smearing due to Rayleigh scattering in aerogel. Because of the small thickness of the aerogel material the emission point uncertainty is negligible for photons produced in aerogel.*

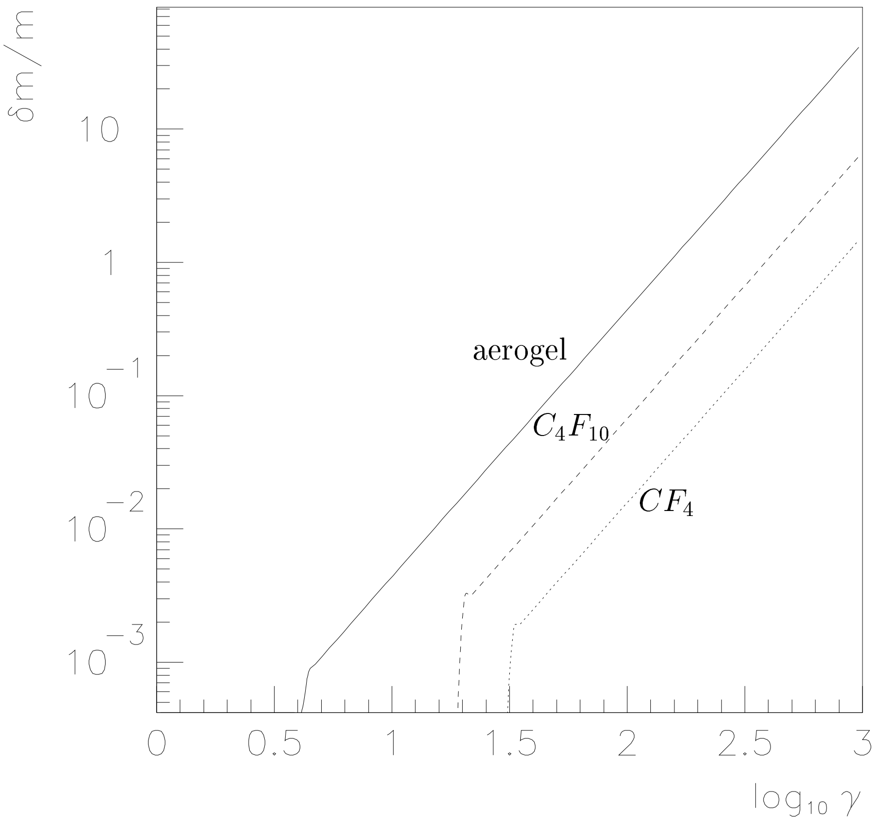

Figure 4: *Calculated resolution of the reconstructed mass after full simulation of the RICH as a function of* γ*. The precision of the* ϑ *reconstruction as well as the mean number of hits per ring image are taken into account. The three curves correspond to the three radiator materials.*

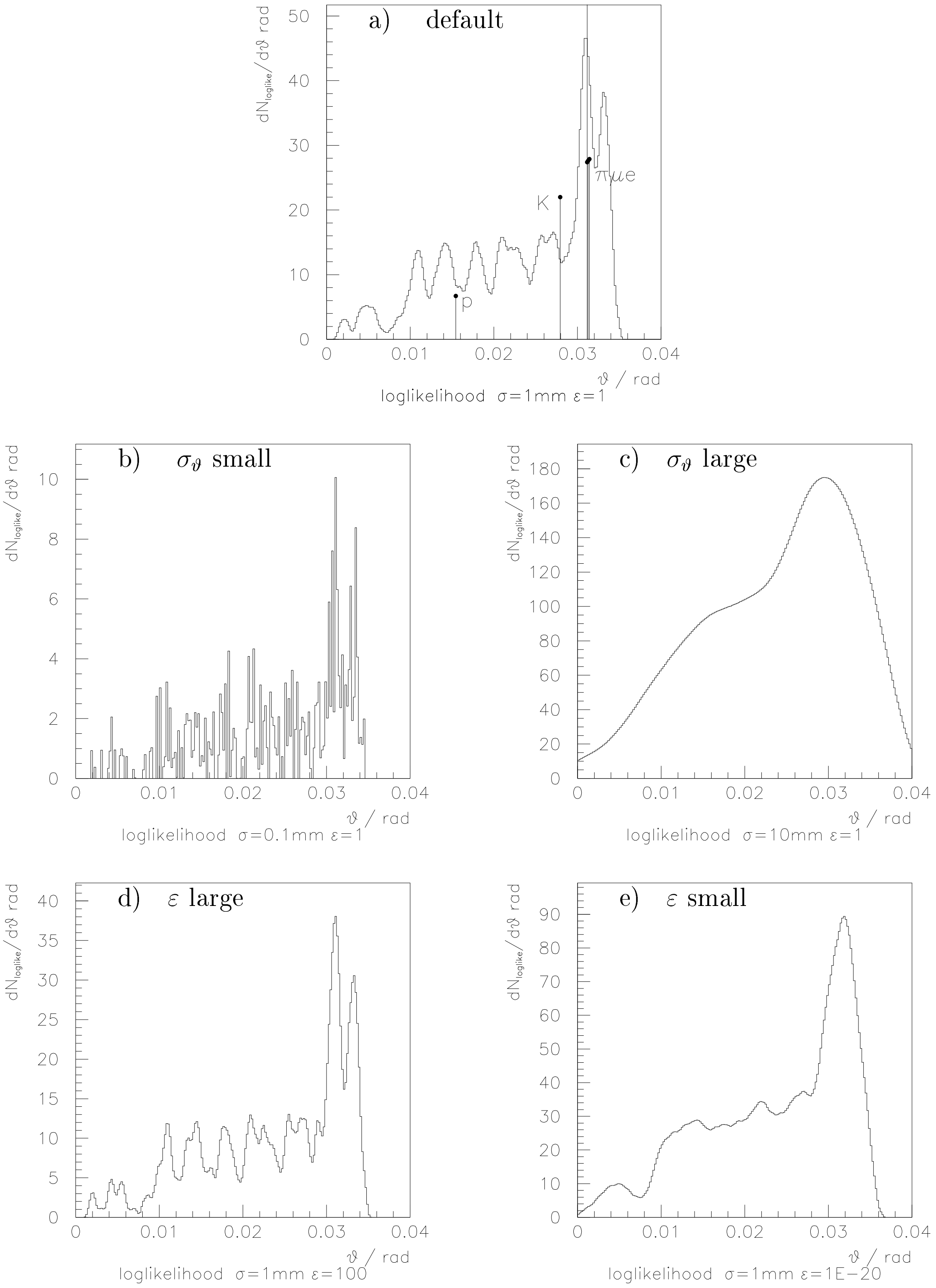

Figure 5: *Log–likelihood function for different sets of the parameter ε and σ_ϑ. The log–likelihood function is shown for a π particle in the RICH2 detector.*

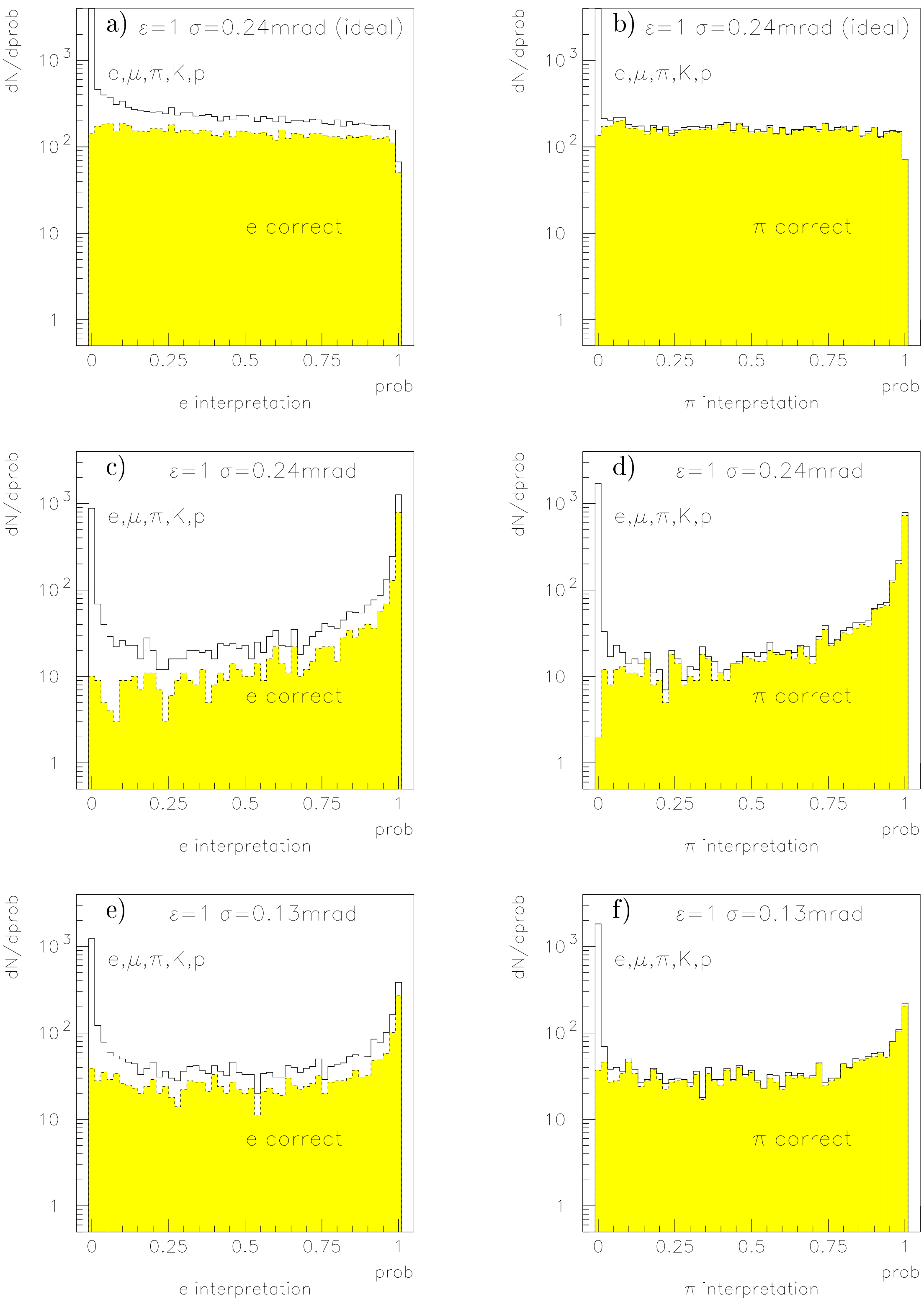

Figure 6: *Probability distribution of the e and π interpretation for all particles and for the correct interpretation (shaded) in the RICH2 detector. Fig. a,b) refer to the ideal case of having only one single track per event. Fig. c-f) show the probability distribution for simulated $B \rightarrow \pi\pi$ events with $\sigma = 0.24\ mrad$ and $\sigma = 0.13\ mrad$.*

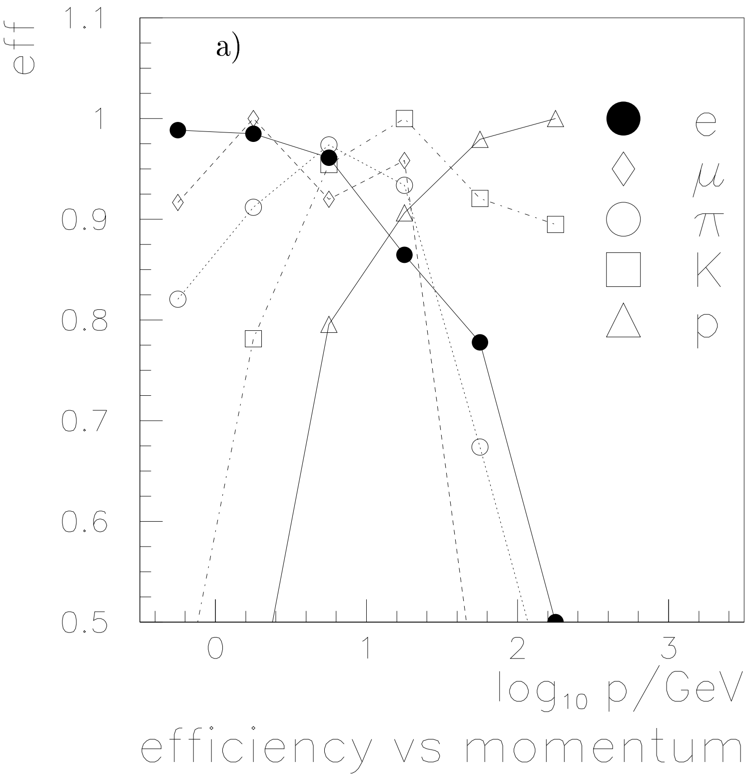

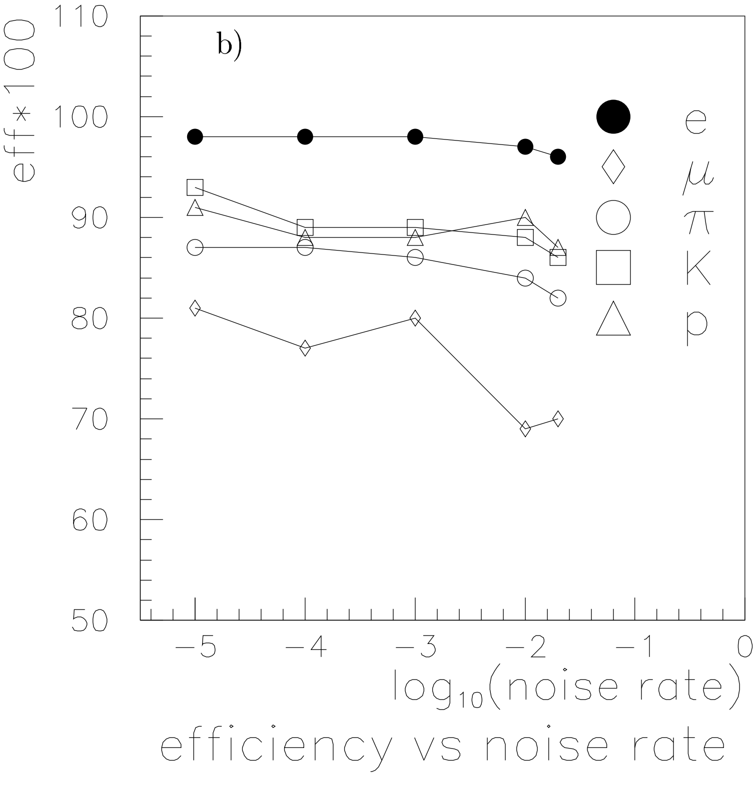

Figure 7: *Efficiencies of the* e, μ, π, K, p *identification a) as function of the momentum of the particle, b) as function of the random noise rate of the pixel.*

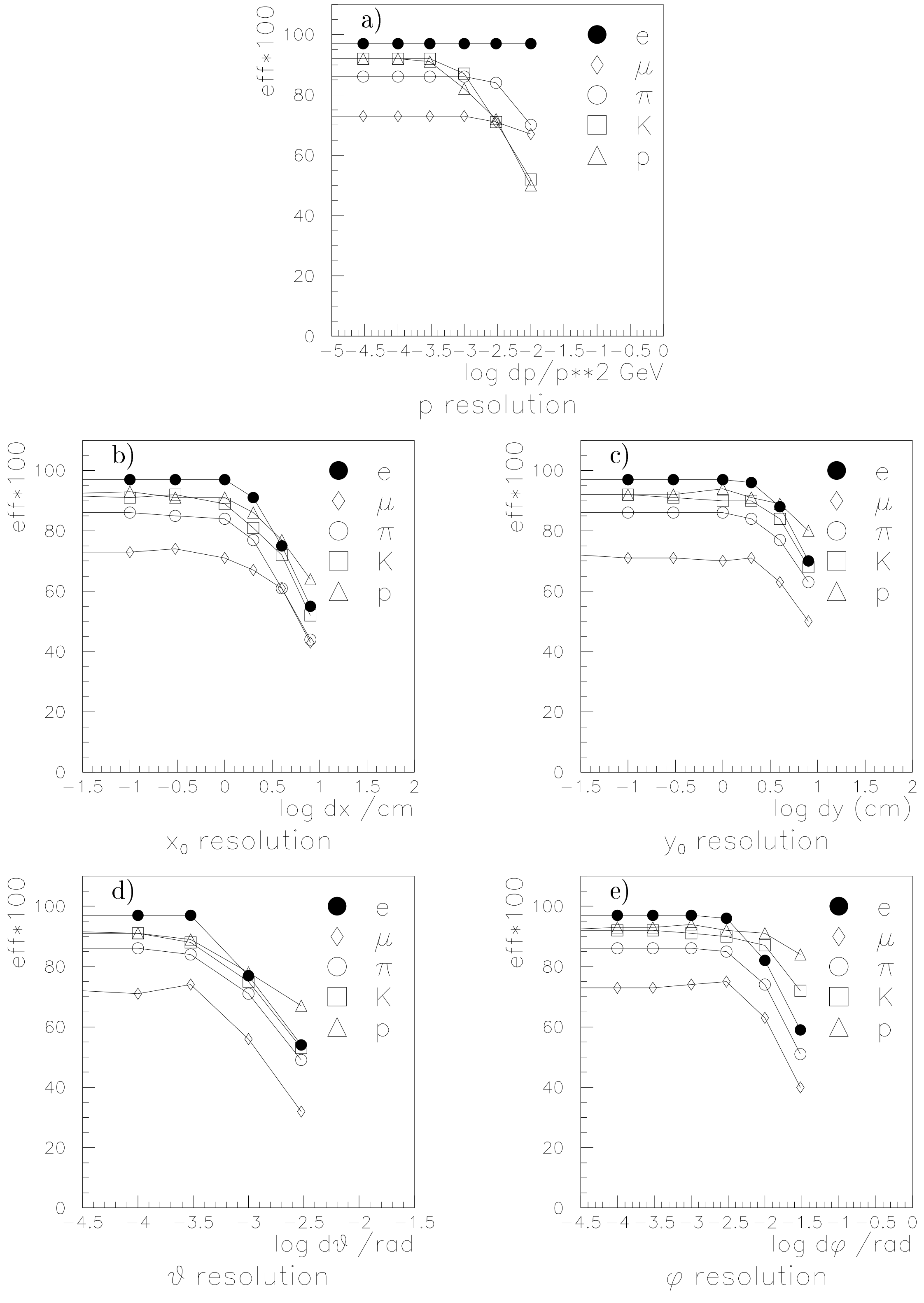

Figure 8: *Efficiencies of the e, μ, π, K, p identification as function of the track parameters: a) the momentum resolution, b) x_0 resolution, c) y_0 resolution, d) ϑ resolution, e) φ resolution.*